ELSEVIER

Contents lists available at ScienceDirect

Acta Materialia

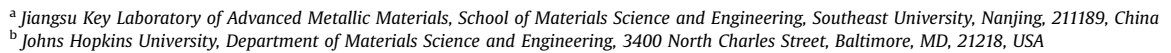
journal homepage: www.elsevier.com/locate/actamat



Full length article

Electrochemical dealloying with simultaneous phase separation

Yuqiao Zeng ^{a, b}, Bernard Gaskey ^b, Ellen Benn ^b, Ian McCue ^b, Gina Greenidge ^b, Kenneth Livi ^b, Xuhai Zhang ^a, Jianqing Jiang ^a, Jonah Elebacher ^{b, *}





ARTICLE INFO

Article history: Received 31 October 2018 Received in revised form 30 March 2019 Accepted 31 March 2019 Available online 6 April 2019

Keywords: Nanoporous Corrosion Nanocomposite Phase separation Dealloying

ABSTRACT

Dealloying is a selective corrosion process during which the more electrochemically active elements in a parent alloy dissolve while the remaining more noble atoms diffuse along the solid-electrolyte interface, resulting in the formation of a nanoporous microstructure composed of core-shell ligaments. In this work, we study an extension of the physics of dealloying in which the parent alloys (Cu–Fe–Mn alloys) contained an engineered composition of elements selected such that, upon dissolution of one of them, the remaining elements phase separate as they become concentrated in the undissolved ligaments. Such simultaneous dealloying and phase separation leads to the formation of rich variety of new porous structures containing nanocomposite ligaments, as well as unanticipated structure evolution such as nanowire growth that are attributed to solution side effects.

© 2019 Acta Materialia Inc. Published by Elsevier Ltd. All rights reserved.

1. Background

Dealloying refers to the intentional selective removal of one or more components from an initially fully dense parent alloy, often electrochemically. Dealloying has been used effectively to fabricate nanoporous metals with three-dimensional, ligament-channel features that have found a variety of applications in catalysis, chemical sensing and electrochemistry [1,2]. Nanoporous metals developed by dealloying binary solid solution alloys such as nanoporous gold (np-Au) from Au—Ag, nanoporous copper (np-Cu) from Cu-Mn, etc., have been extensively investigated [3-7]. In these systems, both the grain morphology and orientation of the precursor alloys are preserved after dealloying. For this reason, dealloying in these simple systems can be described by simple dissolution and diffusion processes on a rigid lattice without considering phenomena such as recrystallization and/or phase separation and a surface diffusion-controlled model is widely accepted to describe the dealloying process and predict the morphology of the resulting porous structure [8.9].

Porosity evolution in the standard dealloying model is controlled by a competition between the rate at which the more

E-mail address: jonah.erlebacher@jhu.edu (J. Elebacher).

noble atoms diffuse along the solid-liquid interface with receding step edges compared to the rate at which the electrochemically more active atoms in terraces are dissolved into the electrolyte. In such a case, a core-shell structure can be obtained in the ligaments as the non-dissolving species accumulate on the surface, especially if the interface diffusion rate is slow. The formation of Au/Au–Cu and Pt/Pt–Ni core-shell metallic ligaments generated by dealloying has been confirmed by three-dimensional atom probe and EDS mapping experiments [10–13].

In Au—Cu and Pt—Ni alloys, both components are miscible across their entire composition range and a solid solution is easily obtained at room temperature. However, if the elements remaining in the ligament display more complex phase behavior, the structure that forms may have more features than a single-phase ligament with a simple composition gradient. A reasonable hypothesis is if the two elements in the ligaments become immiscible as a third element is dissolved, the ligaments will form a phase-separated core-shell structure or some other stable nanocomposite structure. In this work, we use ternary Mn-Fe-Cu alloys as a model system to study the effect of immiscibility in the ligament-forming elements of a dealloyed material on the compositions and microstructures of the resulting nanoporous metals. In Mn-Fe-Cu alloys, Fe and a small amount of Cu can be dissolved in Mn at a temperature above 1000 °C and rapid cooling can maintain a homogenous solid solution structure suitable as a precursor for dealloying. During dealloying, when the Mn atoms with much lower standard electrode potential dissolve preferentially, we expect a phase

^{*} Corresponding author. Maryland Hall 206B, Johns Hopkins University, Department of Materials Science and Engineering, 3400 North Charles Street, Baltimore, MD, 21218, USA.

separation between the remaining Cu and Fe, the solubility of Cu in $\alpha\text{-Fe}$ being quite small with a maximum of 1.8 at% at room temperature.

Due to its importance in industrial applications, the phase separation behavior between Fe and Cu upon annealing and radiation exposure has been intensively studied by both theoretical modeling [14.15] and experiment [16.17]. For instance, Cu precipitation in Fe-rich alloys can be greatly accelerated by irradiation, an effect that plays a significant role in hardening and embrittlement of steels used in high-pressure reactors [18]. The precipitation of small Fe particles in Fe-Cu containing alloys also provides an ideal method to fabricate permanent magnets based on shape anisotropy [19]. The phase separation between Fe and Cu in Fe-rich Fe-Cu alloys during annealing or radiation can be described as a typical spinodal decomposition with the following phase evolution: coherent Cu clusters first precipitate and keep the body-centeredcubic structure of the iron matrix with a radius up to 2 nm. During subsequent growth, these precipitates pass through faulted structures (3R and 9R), and then transform into the face-centeredcubic structure of pure Cu (fcc-Cu), forming a nanocomposite [20,21]. The annealing (radiation) temperature and duration are the most important parameters that determine the characteristic length scale of the nanocomposite.

The phase evolution in Cu-containing low alloy steels during corrosion is quite different from that during annealing or radiation. Rather than forming a bulk nanocomposite, the alloy surface becomes covered by a Cu-rich shell upon exposure to a corrosive environment [22]. The formation of the shell can be explained by a two-step corrosion mechanism: when surrounding Fe atoms are preferentially dissolved by galvanic corrosion, Cu will be removed because the alloy does not contain sufficient Cu to form a continuous network or a fully passivating layer. The Cu atoms dissolve to Cu²⁺ by reduction of dissolved oxygen and then re-deposit onto the substrate through a galvanic displacement reaction with associated oxidation of Fe. Thus a Cu-rich shell is formed on the sample surface and can greatly improve the corrosion resistance of the steel.

In the Mn–Fe–Cu system, it is difficult to predict *a priori* whether the phase segregation of Cu and Fe during dealloying would lead to a nanocomposite structure or core-shell structure based on the contrasting thermal decomposition and corrosion behaviors of the Fe–Cu-containing steels. Therefore, in this work, a series of nanoporous FeCu bimetals were prepared by dealloying $(Mn_{80}Fe_{20})_{100-x}Cu_x$ (at. %, x=0-1). We used HCl solutions of varying concentrations as the dealloying medium, and find a rich phenomenology of resulting microstructures, including ligament formation, phase separation, and redeposition structures such as nanowires, depending on dealloying conditions.

2. Experimental

2.1. Sample preparation

Parent alloys with nominal compositions of $(Mn_{80}Fe_{20})_{100-x}Cu_x$ (at.%, x=0, 0.5, 1.0) were prepared by high frequency induction-melting of Mn, Fe and Cu pure metals (purity > 99%) in a water-cooled copper crucible (Arcast, Inc.) under flowing Ar. The resulting ingots were annealed at approximately $1100\,^{\circ}C$ for 8 h $(Mn_{80}Fe_{20})_{100-x}Cu_x$ precursor alloys described in this paper refer to the annealed alloys. Using a diamond wafering saw, the post-annealed ingots were sliced into samples with a thickness of approximately 2 mm.

Alloy slices were polished with 1200 grit SiC and immersed in HCl solutions for dealloying under free corrosion conditions. The HCl electrolytes were made with 18.3 $M\Omega$ deionized (DI) water and reagent grade HCl. After dealloying, the samples were removed

from the electrolyte and rinsed in acetone to displace the electrolyte. The samples were then dried in air.

2.2. Sample characterization

Optical microscopy observation was performed on both asprepared and annealed ($Mn_{80}Fe_{20}$) $_{100-x}Cu_x$ alloy slices. The metallurgical samples were first polished to a 1 μ m finish with diamond paste and then etched for 90 s in a solution containing 5 g of FeCl₃, 5 ml HCl and 95 ml of C_2H_5OH .

Open-circuit potentials of the $(Mn_{80}Fe_{20})_{100-x}Cu_x$ alloys in HCl solutions were measured using Gamry potentiostats. In the measurement, a saturated Hg/HgCl was used as a reference electrode and a platinum mesh (99.9%, 100 mesh woven from 0.0762 mm wire, Alfa Aesar) as a counter electrode.

The chemical compositions of the dealloyed samples were characterized by energy dispersive X-ray spectroscopy (EDS) and the microstructure was observed by both scanning electron microscopy (SEM, JEOL FEM 2600) and transmission electron microscopy (TEM, FEI, Tecnai G2). The phase evolution was recorded by X-ray diffraction (XRD) with CuK radiation.

3. Results

3.1. Characterization of the precursor alloys

Fig. 1 shows optical micrographs of as-prepared and annealed Mn₈₀Fe₂₀ and (Mn₈₀Fe₂₀)_{99,5}Cu_{0.5}, representative of the Cucontaining Mn-Fe-Cu alloys used in this study). In the annealed samples, except for columnar-like crystals (about 20 µm in width and 50 µm in length), which can also be found in the as-prepared alloys, there are some equiaxed particles with a diameter of about 10 µm. When compared to Mn₈₀Fe₂₀, the annealed Cucontaining alloy has more equiaxed crystals. To clarify whether there is any phase separation in the dealloying precursors, XRD and EDS measurements were performed on the annealed alloys. All the samples exhibit main diffraction peaks at 2θ of 43.0, 45.4 and 47.8 and 54.5°, corresponding to the (221), (310), (311) and (321) planes of the primary cubic Mn (β -Mn, PDF#33-0887), respectively (Fig. 2). There are slightly shifted peaks in the Cu and Fe containing alloy relative to that of pure β -Mn, due to strain introduced by Cu atoms in the lattice. Diffraction signals from fcc-Cu, γ -Fe (fcc), and α -Fe were not found, demonstrating the formation of a single phase in the annealed alloys. EDS mapping further confirms the compositional homogeneity of the annealed Cu-containing alloy (Fig. 3). Together, these observations suggest that the equiaxed grains formed through recrystallization. According to the equilibrium phase diagram, there is a phase transition from γ -Mn to β -Mn at about 1150 °C. The water-cooled copper crucible cannot provide a sufficient cooling rate to maintain the γ -Mn phase and the quick phase transformation from γ -Mn to β -Mn may result in the formation of a large number of defects (dislocations or voids) in the columnar crystals, providing the equiaxed crystals with many inhomogeneous nucleation sites upon annealing. A small amount of Cu added into the Mn₈₀Fe₂₀ alloy might increase defect formation in the as-prepared samples and thus leads to more equiaxed crystals in the annealed specimens.

3.2. Formation of nanocomposite ligaments in nanoporous metals by dealloying

The annealed $(Mn_{80}Fe_{20})_{99.5}Cu_{0.5}$ alloy slices were polished and placed in 1% HCl solution under free corrosion with the duration of 60 min. This process dealloys the sample, removing Mn from it. As can be seen from the bright-field TEM image in Fig. 4 (a), the

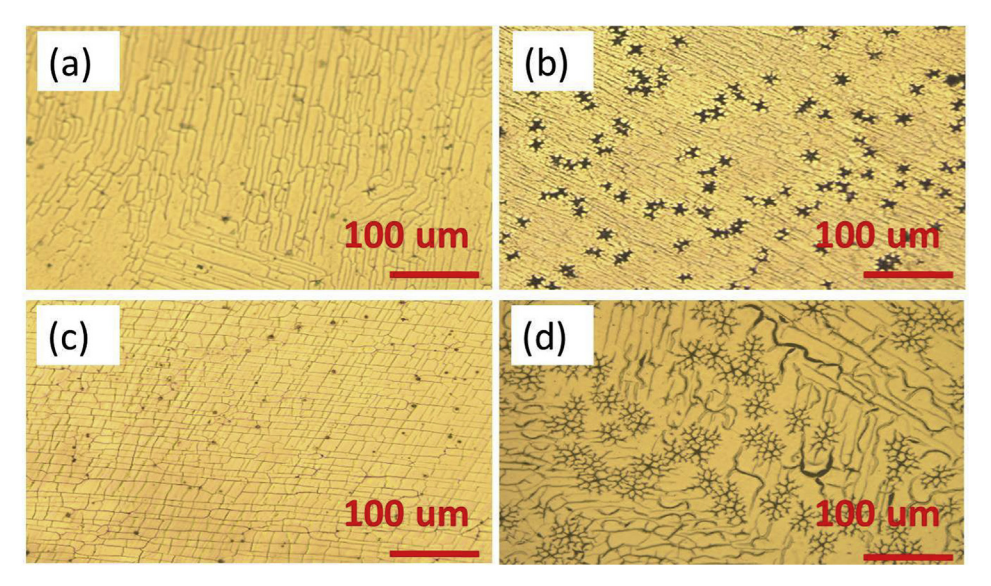


Fig. 1. Metallography of representative alloys used in this study: (a) as-prepared $Mn_{80}Fe_{20}$ (b) as-prepared $(Mn_{80}Fe_{20})_{99.5}Cu_{0.5}$, (c) annealed $Mn_{80}Fe_{20}$ and (d) annealed $(Mn_{80}Fe_{20})_{99.5}Cu_{0.5}$.

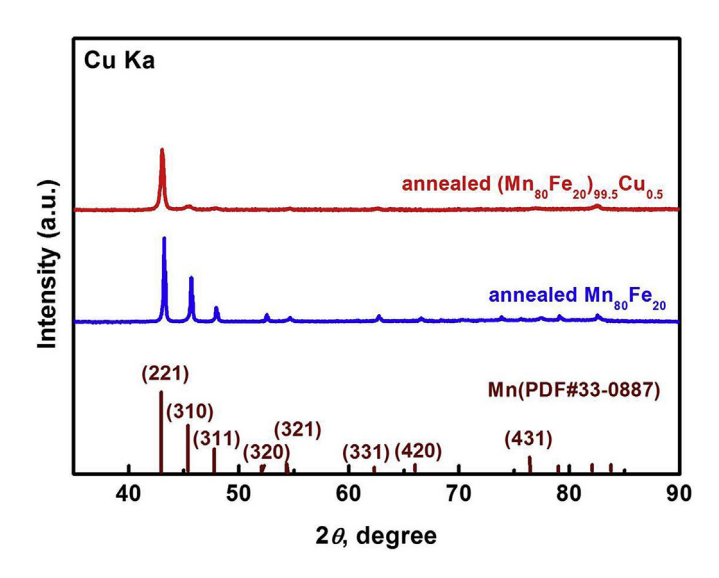


Fig. 2. XRD patterns of the annealed $Mn_{80}Fe_{20}$ and $(Mn_{80}Fe_{20})_{99.5}Cu_{0.5}$ alloys, powder diffraction positions of β-Mn (bcc, PDF#33–0887) are also included for comparison.

dealloyed sample exhibits nanoporosity. The width of the channellike pores is about 5–10 nm, slightly smaller than that of the ligaments (about 10–15 nm). The high resolution TEM micrograph Fig. 4 (b) further reveals that the ligaments are comprised of nanocrystals with an average grain size of about 5 nm. Unlike Au-Ag alloys in which the grain morphology and orientation of the precursor alloys are preserved upon dealloying, nanoporous dealloyed (Mn₈₀Fe₂₀)_{99.5}Cu_{0.5} has a much smaller crystal size than that of the precursor alloy, indicating that there is a recrystallization process during dealloying. This is reasonable because the precursor alloy is a cubic (cub) crystalline material while pure Fe and Cu elements are stable in body-centered cubic (bcc) and face-centered cubic (fcc) structures, respectively, at room temperature. Fig. 4(c) is the selected area electron diffraction (SAED) patterns taken from the dealloyed sample. No reflections of β -Mn can be found. Except for faint peaks from Fe₂O₃/Fe₃O₄ (shown in Figure S1), characteristic diffraction rings of fcc-Cu (220) and α -Fe (211) can be distinguished, demonstrating the formation of composite ligaments upon dealloying. The lattice parameters of Fe and Cu are calculated based on the diffraction results, i.e. 0.287 nm for Fe and 0.362 nm for Cu, respectively, slightly larger than that of the pure $\alpha\text{-Fe}(\text{bcc}, \text{PDF#06}-0696)$ and fcc-Cu (PDF#04-0836). A small amount of Mn residual in Fe and Cu alloys as solid solution may contribute to the lattice expansion.

To further clarify the distribution of Fe and Cu in the dealloyed sample, EDS mapping under a STEM mode was performed on the (Mn₈₀Fe₂₀)_{99.5}Cu_{0.5} alloy dealloyed in 1% HCl solution for 60 min (Fig. 5 (a)). According to the elemental mapping analysis (Fig. 5(c and d)), the dispersion of Fe, Cu and Mn is uniformly homogenous. No Fe—Cu shell-core structure was found in the mapping images. Instead, the specimen displays separated Fe-rich and Cu-rich domains. As indicated by arrows A and B in Fig. 5(c and d), the local area contains a continuous ligament, but the Fe and Cu distributions are discontinuous. Moreover, the compositional domains of the two elements are smaller than the size of individual ligaments and do not overlap, confirming the formation of bimetallic nanocomposite ligaments. The nanocomposite structure observed here differs from both the corrosion products of Cu-containing low alloy steel and leached Al-Cu-Fe alloy. In the steel, after free corrosion, Cu is enriched in the subsurface, forming a core-shell like structure [20]. In the Al–Cu–Fe alloys, dealloying in alkaline solutions leads to a nanoporous Cu structure combined with embedded octahedral Fe_3O_4 particles [23].

3.3. Tailoring structure of Fe—Cu nanoporous metals

As described above, Fe–Cu nanoporous metals with nanocomposite ligaments can be obtained by dealloying the $(Mn_{80}Fe_{20})_{99.5}Cu_{0.5}$ alloy in HCl solution. Further investigations found that the morphology and microstructure of the Fe–Cu nanoporous metals could be tailored by tuning the acid concentration and the compositions of the precursor alloys.

Fig. 6 shows SEM images of the $(Mn_{80}Fe_{20})_{99.5}Cu_{0.5}$ alloy dealloyed in HCl acid solution with different HCl volume concentrations ranging from 0.01% to 30% for 60 min. Dealloying in 0.01% HCl only leads to the formation of a loose passive film without obvious evolution of nanoporosity. Many hexagonal oxides flakes are embedded in the film. In contrast, bicontinuous nanoporous structures can be obtained by dealloying $(Mn_{80}Fe_{20})_{99.5}Cu_{0.5}$ in 0.5%

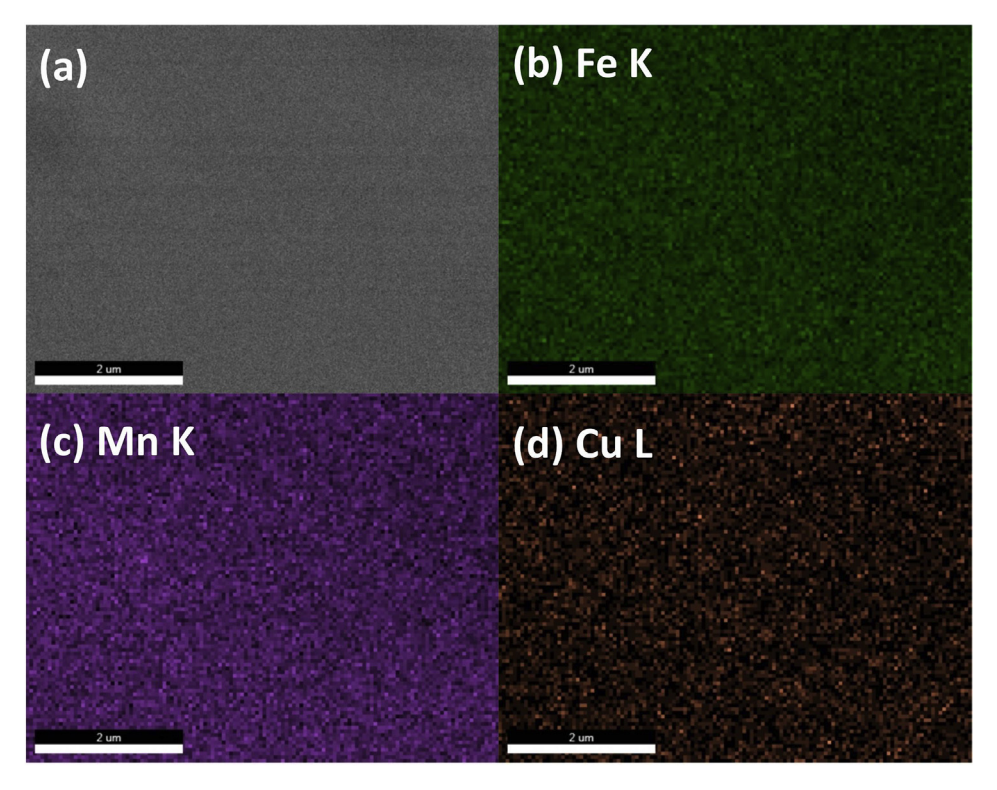


Fig. 3. (a) Back scattered-electron image and the corresponding (b) Fe K,(c)Mn L and (d) Cu L EDS mapping images of the annealed (Mn₈₀Fe₂₀)_{99.5}Cu_{0.5} alloy.

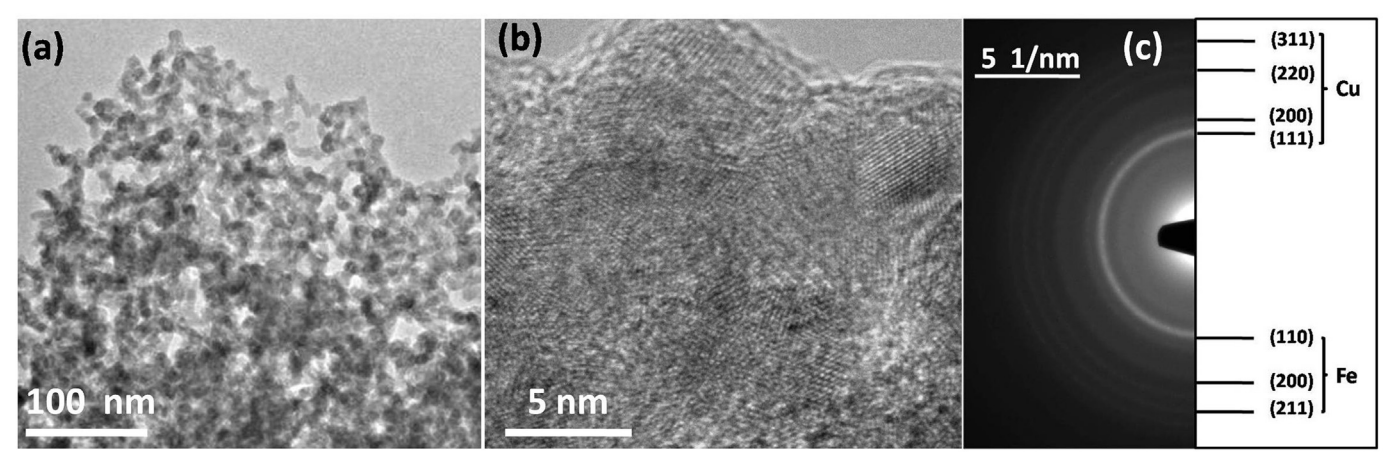


Fig. 4. (a) bright-field, (b) High resolution TEM images and (c) SEAD patterns of the specimen prepared by dealloying (Mn₈₀Fe_{20)99,5}Cu_{0.5} alloy in 1% HCl for 60 min.

and 1% HCl (the sample dealloyed in 0.5% HCl is used as the representative example in Fig. 6(b)). For the sample dealloyed in 5% HCl, Fig. 6(c), the ligament and pore sizes are slightly larger than that dealloyed in 0.5% HCl. Alongside the porous structure, there are some ribbon-like wires with a width of about 150 nm. Further increasing the HCl volume concentration to 30% results in severe corrosion. The size of the alloy decreases rapidly with the formation of a large number of $\rm H_2$ bubbles. After dealloying for 60 min, the sample surface is relatively smooth, whereas there are some coarse porous structures under cracks as indicated by the arrow in Fig. 6(d).

The composition of the precursor alloys also plays a significant role in determining the microstructure of the dealloyed samples. Fig. 7 shows SEM and TEM micrographs of samples prepared by dealloying Mn₈₀Fe₂₀, (Mn₈₀Fe₂₀)_{99,5}Cu_{0.5} and (Mn₈₀Fe₂₀)_{99,0}Cu_{1.0}

alloys in 1% HCl for 60 min. When compared with the dealloyed product of $(Mn_{80}Fe_{20})_{99.5}Cu_{0.5}$, (Fig. 7(c), (d)), the sample prepared by dealloying $Mn_{80}Fe_{20}$ (Fig. 7(a), (b)) nominally exhibit a similar porous structure except that the average sizes of ligaments and pores are 1–2 nm smaller. However, the SAED pattern (inset of Fig. 6 (b)) displays typical bcc rings without any possible signals of fcc-Cu or fcc-Mn. The calculation of the lattice parameter (0.286 nm) based on the SAED patterns suggests that the crystals are Mn-containing α -Fe rather than Mn-rich bcc alloys. Moreover, on the α -Fe (110) ring, there is a clear dark-bright contrast, implying that the Fe crystals are larger than those in the dealloyed $(Mn_{80}Fe_{20})_{99.5}Cu_{0.5}$ material. For dealloyed $(Mn_{80}Fe_{20})_{99.0}Cu_{1.0}$, in addition to the porous structure, the dealloyed sample contained a large number of wires (Fig. 7(e)) similar as those shown in Fig. 6(c). These wires are about 150 nm in width and 20–30 μ m in length. The SAED pattern (inset in

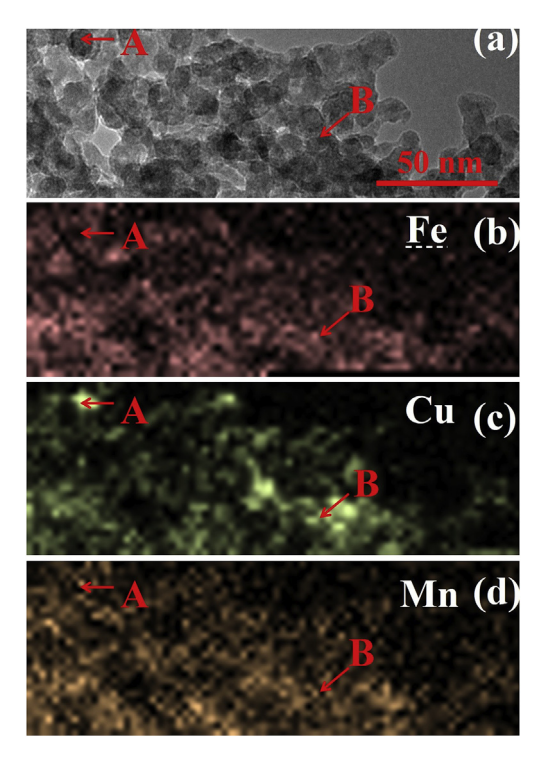


Fig. 5. (a) bright-field TEM image of the $(Mn_{80}Fe_{20})_{99.5}Cu_{0.5}$ alloy dealloyed in 1% HCl for 60 min and the corresponding (b) Fe, (c) Cu and (d) Mn EDS mapping images taken under STEM mode.

lower part of Fig. 6(f)) reveals the wires to be fcc-Cu single crystals. The ligament-channel like porous structure in Fig. 6(f) is much coarser than that obtained in Mn₈₀Fe₂₀ and (Mn₈₀Fe₂₀)_{99.5}Cu_{0.5} alloys. The pores are about 15–20 nm and the ligaments are about 25–30 nm, respectively. The inset in the upper part of Fig. 7(f) is the SAED pattern taken from the porous part, which shows that the ligaments are Fe and Cu nanocomposite materials. When compared to that of the dealloyed (Mn₈₀Fe₂₀)_{99.5}Cu_{0.5} alloy, the diffraction rings of α -Fe are much fainter while the signals of fcc-Cu are brighter,

suggesting a relative decrease in α -Fe content. Moreover, diffraction spots can be clearly seen in the rings of fcc-Cu, demonstrating the formation of fcc-Cu particles with much larger crystal size in the ligaments.

4. Discussion

4.1. Phase separation during dealloying

In general, the process of dealloying solid solutions includes only the selective dissolution of less noble component elements and up-hill diffusion of more noble component elements as they reorganize into a nanoporous microstructure. In the Mn-Fe-Cu system, however, phase separation is also involved, i.e., the MnFeCu solid solution with a β -Mn structure decomposes to Fe(Mn) (α -Fe(Mn)) and CuMn (fcc-Cu). It is not clear yet precisely when the phase separation takes place during dealloying and how it effects the formation of nanoporous structure. To clarify this, the Mn₈₀Fe₂₀ and (Mn₈₀Fe₂₀)_{99.5}Cu_{0.5} alloys were placed in a 1% HCl solution for 5–120 min. Open circuit potential (OCP)-time measurements were performed on these alloys to examine the potential change during dealloying because corrosion under these conditions are similar to free corrosion. Fig. 8 displays the OCP curves with time. During the entire duration of the test, the Cu-containing specimen displayed a more anodic potential than the specimen without. This suggests that the presence of Cu influences the kinetics of the anodic reaction (dealloying), providing the alloy with a more stable surface. For both alloys, the corrosion behavior can be divided into three different potential stages. During the first minutes of immersion, the OCP increases rapidly. From its maximum, the OCP exhibits a rapid decrease, followed by another increase, forming a V-shaped curve from 10 min to 30 min. The local most negative potential sits between -0.73 and -0.75 V. After this period, the potential only varies slowly. The OCP of the Mn₈₀Fe₂₀ alloy decreases slightly and approaches a relatively steady-state value of -0.73 V at 120 min. In contrast, the OCP of the $(Mn_{80}Fe_{20})_{99.5}Cu_{0.5}$ alloy increases to -0.67 V. For a variation of OCP with corrosion time, similar behavior has been observed in some carbon steels and Cu-bearing steels which undergo pitting corrosion [24]. Usually, the initial growth, breakdown and partial repair of a corresponding passive

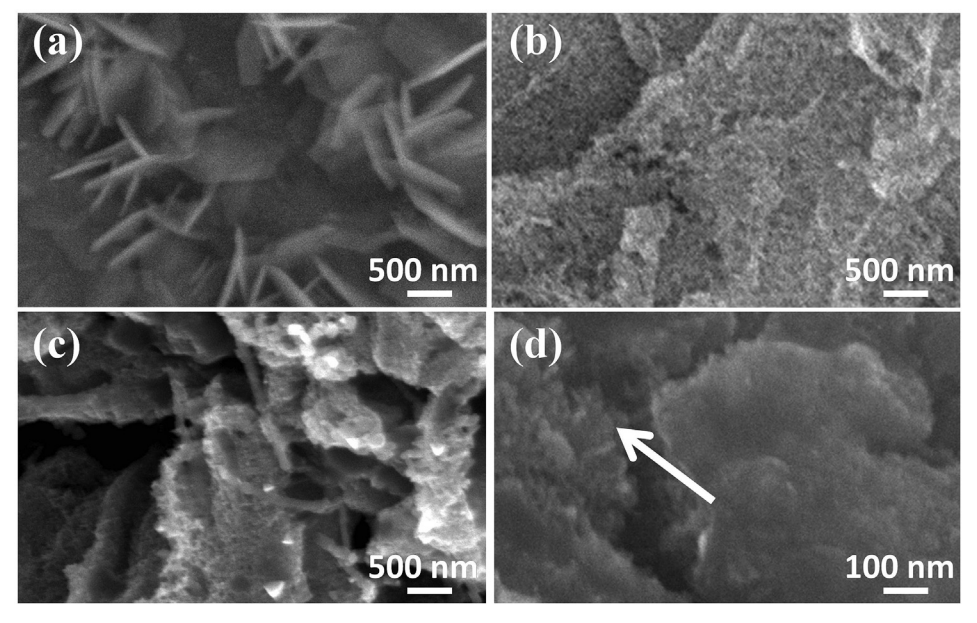


Fig. 6. SEM images of the $(Mn_{80}Fe_{20})_{99.5}Cu_{0.5}$ alloy dealloyed in HCl with a volume concentration of (a) 0.01%, (b) 0.5%, (c) 5% and (d) 30% for 60 min.

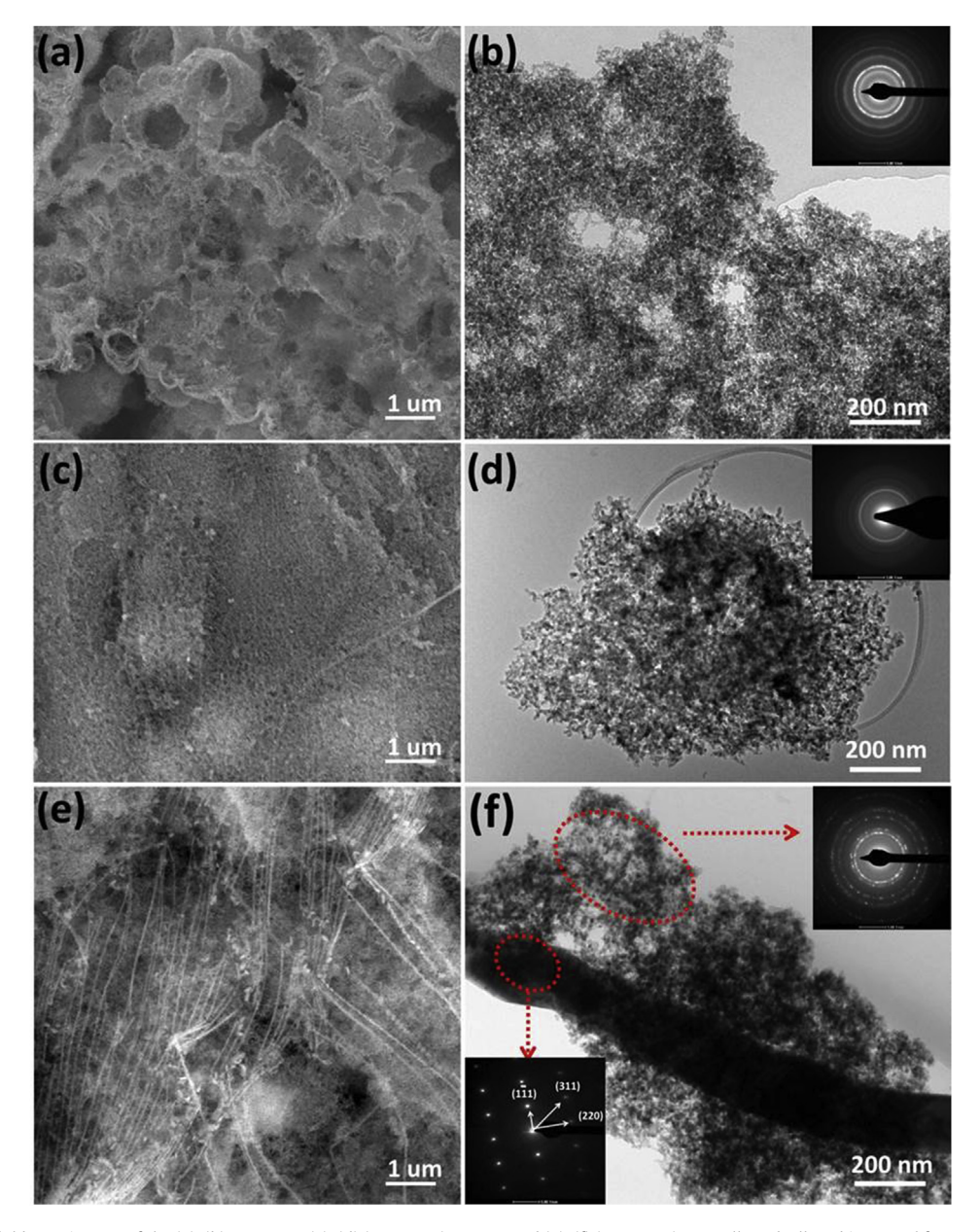


Fig. 7. SEM and bright-field TEM images of the (a), (b) $Mn_{80}Fe_{20}$, (c), (d) $(Mn_{80}Fe_{20})_{99.5}Cu_{0.5}$ and (e), (f) $(Mn_{80}Fe_{20})_{99}Cu_1$ alloys dealloyed in 1% HCl for 60 min. The insets in (b), (d), (f) are the corresponding SEAD patterns of the bright-field images.

film are used to explain such OCP changes. However, the variation of the OCP in these steels is only about 0.02 V, much smaller than that observed in dealloying $Mn_{80}Fe_{20}$ and $(Mn_{80}Fe_{20})_{99.5}Cu_{0.5}$ alloys.

To examine the OCP behavior further, samples were dealloyed to the interesting inflection points on the OCP-time curves (0 min, 5min, 10 min, 20 min, 60 min and 120 min) to examine phase and morphology development. XRD diffraction peaks in the 2θ range of $40-50^\circ$ as a function of dealloying time are shown in Fig. 9. For the Mn₈₀Fe₂₀ alloy, the initial structure has three main peaks with high intensity, corresponding to the (221), (310) and (311) planes of β -Mn. After 5 min of corrosion, the original diffraction peaks have completely disappeared and a contribution from (110) planes of α -Fe appears as a new broad peak, indicating a fast phase transition from cub-Mn to α -Fe. The broad feature is centered at 2θ of 44.41°, lower than that of the pure α -Fe. This suggests that there is still a significant amount of Mn atoms expanding the bcc-Fe lattice. The

(110) α -Fe peak shifts significantly and continuously to higher angles at corrosion time up to 20 min. After that, the shift is not noticeable, as the process of stripping Mn atoms from the bcc-Fe crystals slows down. The (110) peak finally reaches a steady value of 44.659° when the alloy is dealloyed for 60 min. It can be seen that the phase transformation during dealloying the Mn₈₀Fe₂₀ alloy evolves only β -Mn and α -Fe. For the (Mn₈₀Fe₂₀)_{99.5}Cu_{0.5} alloy, the XRD evolution with dealloying duration is similar, i.e., the (221), (310) and (311) planes of β -Mn are replaced by the (110) planes of α -Fe after 5 min of dealloying. The (111) α -Fe peak shifts towards 2θ of 44.659° until 60 min of dealloying. However, it should be noted that besides the broad (111) α -Fe peak, there is a small peak centered at 43.101° that appears after 5 min of dealloying. This peak position is expected for fcc-Cu (111); the lower 2θ compared to pure fcc-Cu indicates that the Cu phase formed here also contains significant Mn. We conclude that the phase separation between Fe and Cu takes place quickly. As the dealloying time increases, the fcc-Cu

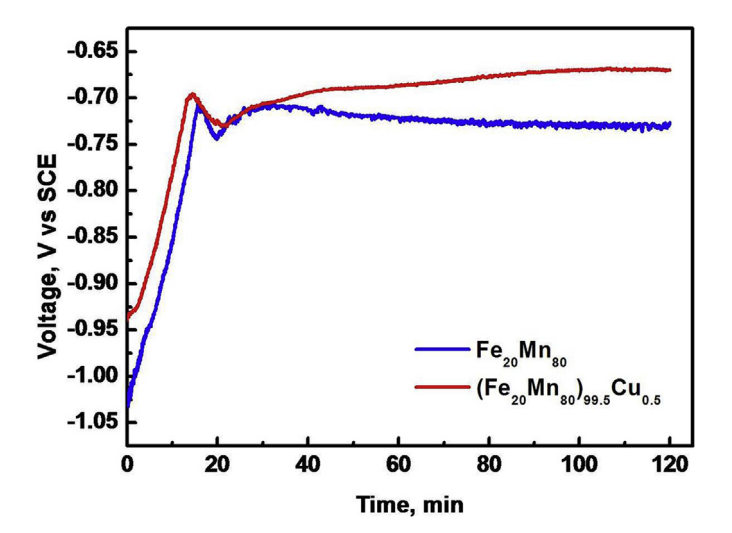


Fig. 8. OCP-time curves of $Mn_{80}Fe_{20}$ and $(Mn_{80}Fe_{20})_{99.5}Cu_{0.5}$ alloys in 1% HCl.

(111) peak moves to higher angle, consistent with decreasing residual Mn content. Meanwhile, the diffraction intensity of fcc-Cu (111) grows at the expense of the α -Fe peak, indicating the increasing relative abundance of fcc-Cu phase in the developing nanoporous structure. The increase in Cu exposed to the electrolyte explains the positive shift in OCP after 20 min of dealloying.

The micromorphology of both Mn $_{80}$ Fe $_{20}$ and (Mn $_{80}$ Fe $_{20}$) $_{99.5}$ Cu $_{0.5}$ alloys change greatly upon corrosion in HCl solution. Large amounts of hydrogen bubbles continuously form at the sample surfaces and the specimens gradually lose their metallic luster and eventually become black. Fig. 10 displays the microscopic surface morphology development (SEM images) of the Mn $_{80}$ Fe $_{20}$ and (Mn $_{80}$ Fe $_{20}$) $_{99.5}$ Cu $_{0.5}$ specimens upon dealloying in 1% HCl for different periods of time. For both alloys, after 5 min of dealloying, a large number of cracks appear along the β -Mn crystal boundary, suggesting that the alloys initially experienced severe intergranular corrosion. In the island-like areas surrounded by these cracks, the

surface is relatively smooth and no porous structures are found in these samples. The further increase in dealloying time to 10 min does not cause a distinctive change except some local flaking off of a few islands. Underneath, similar smooth and dense islands with cracks can be seen, suggesting that the formation, growth, breakdown and partial repair of passive layers is the dominant effect during this period of time. After 20 min of dealloving, the surface becomes much rougher and the islands can barely be distinguished from each other. However, a clear porous structure still cannot be seen. After dealloying for 60 min, some three-dimensional, ligament-channel nanoporous features appear on both of the sample surfaces. The extension in dealloying duration to 120 min does not cause significant coarsening of the nanoporous structure for the Mn₈₀Fe₂₀ alloy. In the copper containing sample, the ligament size increases and the growth of Cu nanowires was observed in some areas after 120 min (Figure S2).

Taking the OCP, XRD and SEM observations together, we conclude that phase decomposition from the parent β -Mn phase to nanocrystalline α -Fe and fcc-Cu takes place far before the formation of the nanoporous microstructure. Interestingly, according to the equilibrium Fe—Mn phase diagram, when the Mn content decreases from 80 at. % to lower than 50 at. %, the stable phase of Fe at room temperature should be γ -Fe, with α -Fe existing only when the Mn content is lower than 5 at. %. However, in this study, the XRD results show that Fe from β -Mn transforms directly into α -Fe. This observation can explain why the separation between Cu and Fe takes place rapidly, with the Cu solubility in α -Fe being much lower than that in either β -Mn or γ -Fe.

4.2. Formation and coarsening of nanocomposite ligaments

The $(Mn_{80}Fe_{20})_{100-x}Cu_x$ system exhibits some characteristic features during the formation and coarsening of a nanoporous structure:

 A homogenous nanoporous structure can be obtained even when there is a phase separation of Cu and Fe before the development of nanoporosity. For most other precursor alloys

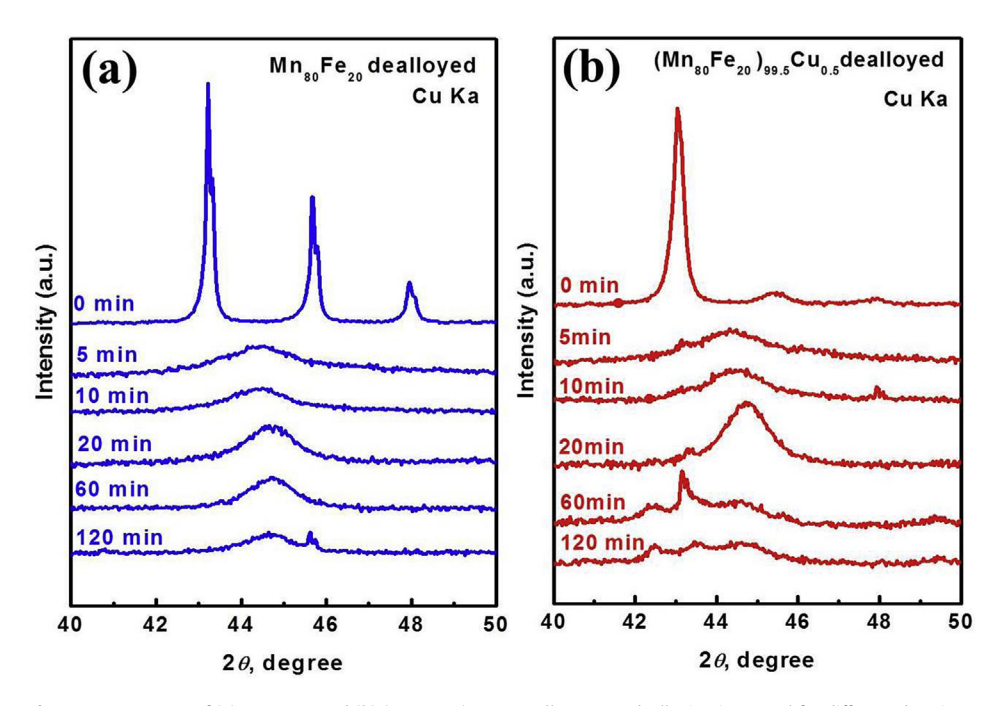


Fig. 9. XRD patterns of (a) $Mn_{80}Fe_{20}$ and (b) $(Mn_{80}Fe_{20})_{99.5}Cu_{0.5}$ alloys upon dealloying in 1% HCl for different durations.

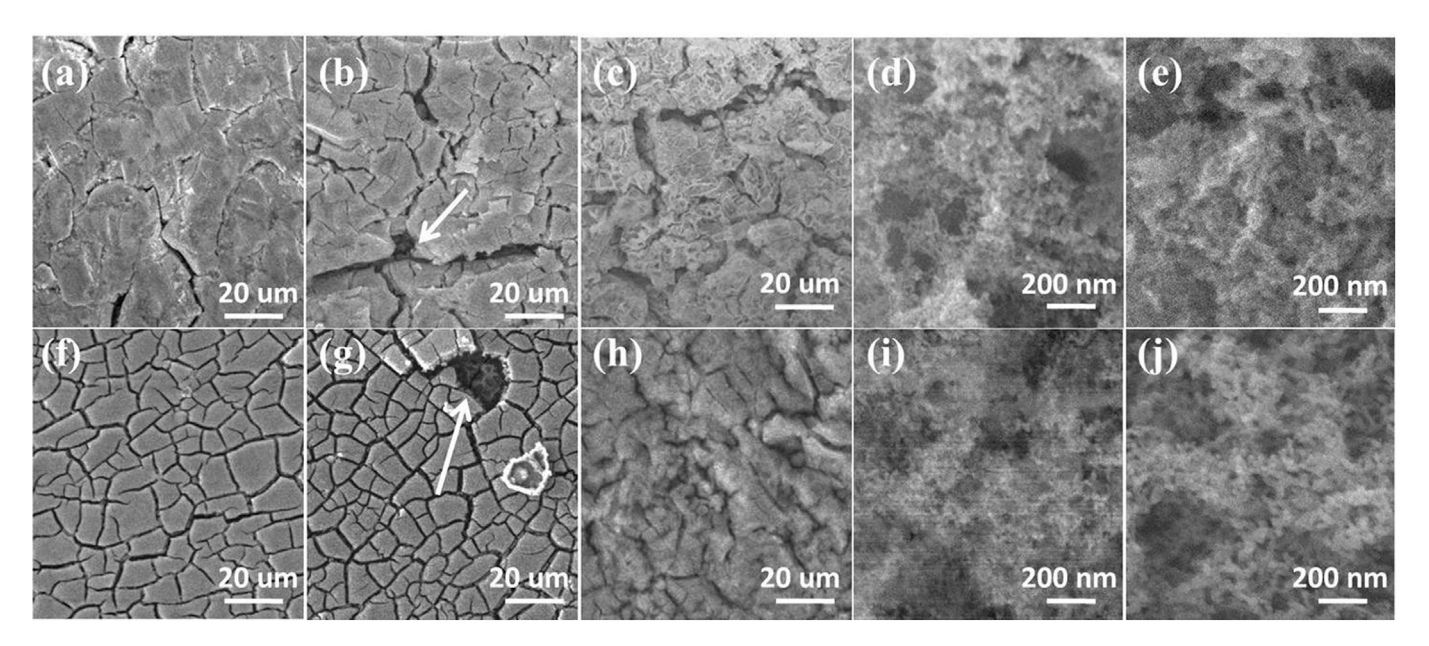


Fig. 10. SEM images of (a) Mn₈₀Fe₂₀ and (b) (Mn₈₀Fe₂₀)_{99.5}Cu_{0.5} alloys upon dealloying in 1% HCl for different durations.

that contain multiple phases, dealloying either leads to a selective dissolution of one phase, such as the corrosion of pearlite in HCl, where α -Fe dissolves and a three-dimensional nanoporous structure cannot form, or results in an inhomogeneous nanoporous structure [25].

- 2) The ligaments in the porous structure are composed of bimetal nanocomposite. Under normal conditions, when the sacrificial elements dissolve during dealloying, the more noble elements will accumulate at the interface, forming a core-shell structure with the surface enriched in the nobler element and the center retaining similar composition to the precursor alloy. Nanocomposite ligaments from an initially homogenous precursor have not been reported before.
- 3) The formation of nanoporosity from (Mn₈₀Fe₂₀)_{100-x}Cu_x is quite sensitive to the electrolyte concentration, precursor composition and corrosion time. By changing these parameters, three different morphologies were obtained, including homogenous nanoporous Fe—Cu bimetals (e.g., Fig. 3(a and b)), nanoporous bimetals with Cu nanowires (e.g., Fig. 6(e)) and surfaces without pores (e.g., Fig. 3(a)).

Usually, alloys that form homogeneous nanoporous structure through dealloying, such as Au—Ag, Cu—Mn and Pt—Ni alloys, share four basic characteristics: 1) the sacrificial elements in the precursor alloys have much higher electrochemical activity than the more noble element; 2) the atomic content of the sacrificial elements in the precursor alloys should be higher than 50%; 3) the precursor alloy is homogeneous with no phase separation; 4) diffusion of the non-dissolving elements at the alloy/electrolyte interface must be sufficiently fast. In this study, the (Mn₈₀Fe₂₀)_{100-x}Cu_x system satisfies most of these requirements. The exceptions are: 1) phase separation between Cu and Fe takes place before the nanoporous structure develops; 2) Fe plays a dual role as both sacrificial and non-dissolving element at different phases of the dealloying process.

Based on these considerations, a model shown in Fig. 11 is used to explain the characteristics dealloying behavior of $(Mn_{80}Fe_{20})_{100-x}Cu_x$. First, fast leaching of Mn from the alloy leads to the phase decomposition from β -Mn to nanocrystalline α -Fe and fcc-Cu. The

newly formed nanocrystalline composite has extremely low fcc-Cu content, different from pearlite where the Fe₃C phase (nobler phase) always has higher than 8-9 at. % phase content. In such a case, selective dissolution of one phase cannot take place and corrosion of $(Mn_{80}Fe_{20})_{100-x}Cu_x$ will be similar to that of pure FeMn alloys, i.e., Mn dissolves as a sacrificial element, while both Fe and Cu remain. At this point, nanoporosity begins to evolve with nanocomposite ligaments. In the ligaments. Fe and Cu-rich areas are homogenously dispersed. Though the diffusion rates of Cu at the Cu/electrolyte interface and Fe at the FeMn/electrolyte interface are high enough to form continuous ligaments, due to the limited solubility of fcc-Cu in α -Fe, diffusion of Cu through α -Fe or on α -Fe surfaces is hindered. Thus, core-shell structures do not form. When most of the Mn atoms are leached, α -Fe(Mn) will lose the anodic protection from Mn. Fe will then begin to dissolve as well, preferentially to the fcc-Cu(Mn) domains. Because the fcc-Cu phase content is insufficient to form a continuous network of pure Cu ligaments, Cu domains become detached from the structure as the connected Fe-rich domains are attacked. The disconnected Cu can then dissolve, and Cu²⁺ re-deposits onto the un-attacked Cu ligaments through a galvanic reaction associated with the oxidation of Fe. This dissolution and redeposition allows Cu to migrate from the original separated domains, forming pure Cu nanowires. For precursor alloys with higher Cu content, the dissolution rate of Cu²⁺ will increase resulting in the formation of a higher density of nanowires during dealloving.

When the HCl concentration is at or below 0.01%, the limited availability of H^+ cannot sustain the sudden pH increase near the solid-liquid surface caused by fast dissolution of Mn from the precursor alloy. Therefore the elemental electrochemical potential of Fe and Mn at the sample surface will shift more negative, making the oxidation of Mn/Fe by dissolved O_2 in the electrolyte possible $(2Mn + O_2 + 2H_2O \rightarrow 2Mn(OH)_2$, $2Fe + O_2 + 2H_2O \rightarrow 2Fe(OH)_2$). A fully oxidized surface is thus observed.

When the HCl concentration is above 30%, in addition to the accelerated selective corrosion rate and coarsening rate, the reaction $2Cu+4HCl\rightarrow 2H(CuCl_2)+H_2$ can take place on Cu ligaments resulting in a smooth surface with highly coarsened porous structure underneath.

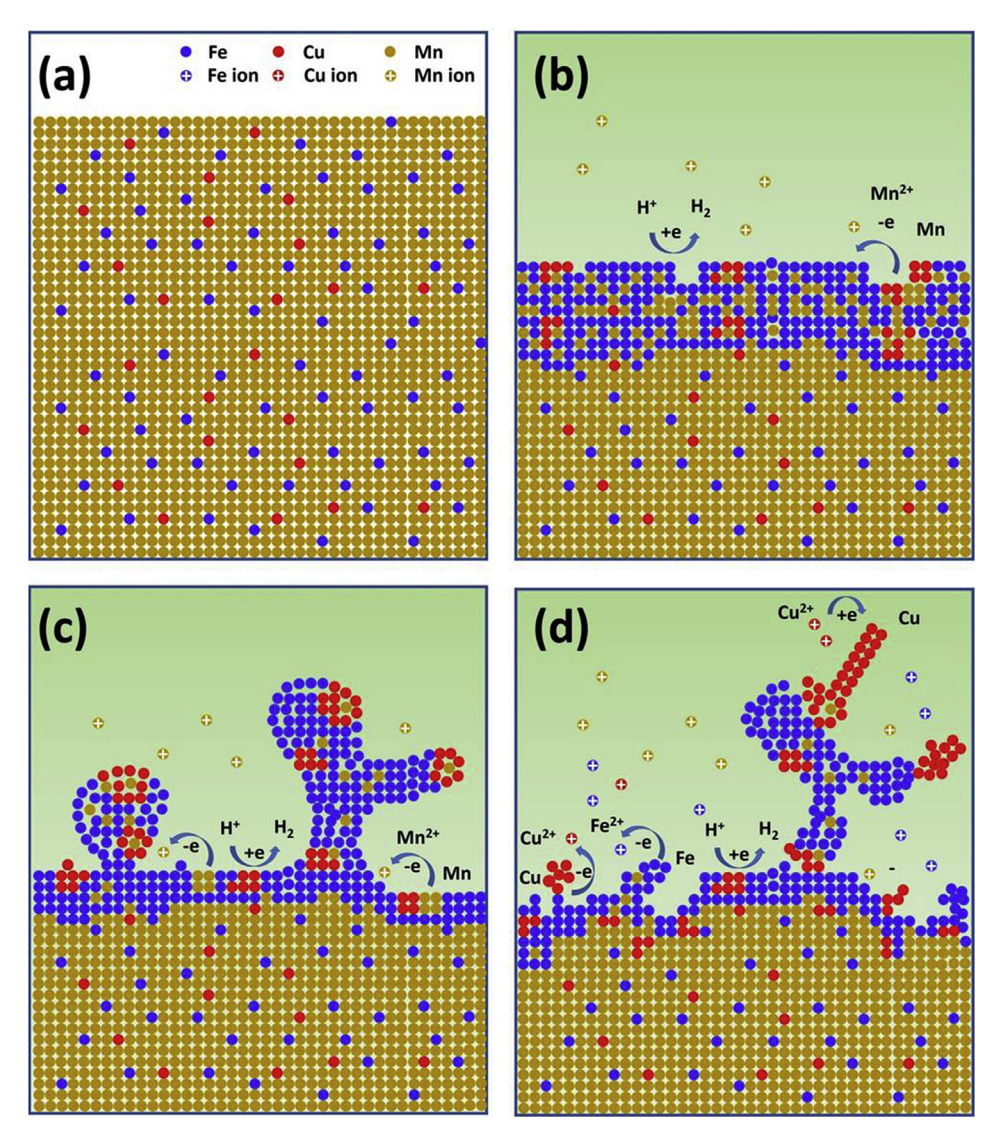


Fig. 11. Atomistic description of the dealloying mechanism for $(Mn_{80}Fe_{20})_{100-x}Cu_x$ alloys, (a) schematic of the MnFeCu solid solution (β–Mn), (b) phase separation between FeMn (α-Fe) and CuMn(fcc-Cu) when some Mn atoms are initially removed, (c) formation of a nanoporous structure with nanocomposite α-Fe and fcc-Cu ligaments during the further leaching of Mn, (d) α-Fe starts to be selectively dissolved when the nanoporous structure starts coarsening; fcc-Cu nearby loses connectivity and stability, are dissolved and then redeposit onto the un-attacked Cu ligaments through a galvanic reaction.

5. Conclusions

In this work, a series of (Mn₈₀Fe₂₀)_{100-x}Cu_x (at%, x = 0–1.0) solid solutions were dealloyed in HCl acid solutions with various concentrations. It was found that phase separation between α -Fe and fcc-Cu occurs before the development of a nanoporous structure. When the HCl concentration is lower than 0.01% or higher than 30%, continuous three-dimensional, ligament-channel features could not be obtained. When the HCl concentration is 0.5–5%, nanoporosity with nanocomposite α -Fe and fcc-Cu ligaments evolved. During coarsening, α -Fe dissolves and Cu nanowires grow. The phase separation and the double role played by Fe, both forming ligaments and dissolving at different phases in the dealloying process, led to the characteristic features formed during dealloying (Mn₈₀Fe₂₀)_{100-x}Cu_x.

The phase separation between Cu and Fe in the initial stages of dealloying produces domains smaller than the length scale of the ligaments which subsequently evolve, resulting in a network of nanocomposite ligaments with stable, nearly pure Cu and Fe domains. By tailoring the precursor alloy and carefully selecting of the

dealloying process parameters, this unique structure was achieved in a single dealloying step combining phase separation with electrochemical dissolution to create a material with both geometric and compositional nanostructure.

Acknowledgements

This work was supported by the Hwa Ying Culture & Education Foundation; the National Science Foundation of China [grant numbers 51771052; And the Fundamental Research Funds for the Central Universities [grant numbers 2242018K41056]. JDE thanks the National Science Foundation for supporting dealloying work in his laboratory under grant DMR-1806342.

Appendix A. Supplementary data

Supplementary data to this article can be found online at https://doi.org/10.1016/j.actamat.2019.03.039.

References

- Y. Ding, M.W. Chen, Nanoporous metals for catalytic and optical applications, MRS Bull. 34 (2009) 569–576.
- [2] I. McCue, E. Benn, B. Gaskey, J. Erlebacher, Dealloying and dealloyed materials, Annu. Rev. Mater. Res. 46 (2016) 263—286.
- [3] A.J. Forty, Corrosion micromorphology of noble metal alloys and depletion gilding, Nature 282 (1979) 597–598.
- [4] Y. Ding, Y.J. Kim, J. Erlebacher, Nanoporous gold leaf: "Ancient technology"/ advanced material, Adv. Mater. 16 (2004) 1897—1990.
- [5] L.H. Qian, M.W. Chen, Ultrafine nanoporous gold by low-temperature dealloying and kinetics of nanopores formation, Appl. Phys. Lett. 91 (2007), 083105
- [6] S.V. Petegem, S. Brandstetter, R. Maass, A.M. Hodge, B.S. El-Dasher, J. Biener, B. Schmitt, C. Borca, H.V. Swygenhoven, On the microstructure of nanoporous gold: an x-ray diffraction study, Nano Lett. 9 (2009) 1158–1163.
- [7] J.R. Hayes, A.M. Hodge, J. Biener, A.V. Hamza, K. Sieradzki, Monolithic nanoporous copper by dealloying Mn-Cu, J. Mater. Res. 21 (2006) 2611–2616.
- [8] J. Erlebacher, M.J. Aziz, A. Karma, N. Dimitrov, K. Sieradzki, Evolution of nanoporosity in dealloying, Nature 410 (2001) 450–453.
- [9] J. Erlebacher, An atomistic description of dealloying porosity evolution, the critical potential, and rate-limiting behavior, J. Electrochem. Soc. 151 (2004) C614—C626.
- [10] T. Fujita, P. Guan, K. McKenna, X.Y. Lang, A. Hirata, L. Zhang, T. Tokunaga, S. Arai, Y. Yamamoto, N. Tanaka, Y. Ishikawa, N. Asao, Y. Yamamoto, J. Erlebacher, M.W. Chen, Atomic origins of the high catalytic activity of nanoporous gold, Nat. Mater. 11 (2012) 775–779.
- [11] L. Gan, M. Heggen, R. O'Malley, B. Theobald, P. Strasser, Understanding and controlling nanoporosity formation for improving the stability of bimetallic fuel cell catalysts, Nano Lett. 13 (2013) 1131–1138.
- [12] F. Soisson, C.C. Fu, Cu-precipitation kinetics in α-Fe from atomistic simulations: vacancy-trapping effects and Cu-cluster mobility, Phys. Rev. B 76 (2007) 214102.
- [13] C. Zhang, L.H. Qian, K. Zhang, S.L. Yuan, J.W. Xiao, S. Wang, Hierarchical porous Ni/NiO core-shells with superior conductivity for electrochemical pseudocapacitors and glucose sensors, J. Mater. Chem. 3 (2015) 10519–10525.

- [14] S. Xiao, F. Xiao, Y. Hu, S.L. Yuan, S. Wang, L.H. Qian, Y.Q. Liu, Hierarchical nanoporous gold-platinum with heterogeneous interfaces for methanol electrooxidation, Sci. Rep. 4 (2014) 4370.
- [15] M.H. Mathon, A. Barbu, F. Dunstetter, F. Maury, N. Lorenzelli, C.H. de Novion, Experimental study and modelling of copper precipitation under electron irradiation in dilute FeCu binary alloys, J. Nucl. Mater. 245 (1997) 224–237.
- [16] F. Mauryt, N. Lorenzellit, M.H. Mathont, C.H. de Noviont, P. Lagardel, Copper precipitation in FeCu, FeCuMn, and FeCuNi dilute alloys followed by x-ray absorption spectroscopy, Phys.: Condenr. Matter 6 (1994) 569–588.
 [17] T. Ujiro, S. Satoh, R.W. Staehle, W.H. Smyrl, Effect of alloying Cu on the
- [17] T. Ujiro, S. Satoh, R.W. Staehle, W.H. Smyrl, Effect of alloying Cu on the corrosion resistance of stainless steels in chloride media, Corros. Sci. 43 (2001) 2185—2200.
- [18] P. Soulat, Y. Meyzaud, Prevention of fast fracture in pressurized water nuclearpower plants, Mem. Et. Sci. Rev. M&IL, 87 (1990) 769–784.
- [19] V. Kuncser, M. Valeanu, F. Lifei, D. Predoi, A. Jianu, W. Kappel, M. Codescu, E. Patroi, I. Pasuk, M. Bulinski, G. Filoti, Micro-structure and magnetic properties of Fe—Cu nanocomposites for anisotropic permanent magnets, J. Alloy. Comp. 395 (2005) 1—6.
- [20] J. Othen, M.L. Jenkins, G.D.W. Smith, High-resolution electron microscopy studies of the structure of Cu precipitates in α -Fe, Philos. Mag. A 70 (1994) 1–24.
- [21] P.J. Othen, M.L. Jenkins, G.D.W. Smith, W.J. Phythian, Transmission electron microscope investigations of the structure of copper precipitates in thermallyaged Fe-Cu and Fe-Cu-Ni Philos, Magn. Lett. 64 (1991) 383—391.
- [22] J.H. Hong, S.H. Lee, J.G. Kim, J.B. Yoon, Corrosion behavior of copper containing low alloy steels in sulphuric acid, Corros. Sci. 54 (2012) 174—182.
- [23] Z. Qi, Y. Gong, C. Zhang, J.L. Xu, X.G. Wang, C.C. Zhao, H. Ji, Z.H. Zhang, Fabrication and characterization of magnetic nanoporous Cu/(Fe,Cu)₃O₄ composites with excellent electrical conductivity by one-step dealloying, J. Mater. Chem. 21 (2011) 9716–9724.
- [24] E.E. Oguziea, J.B. Li, Y.Q. Liu, D.M. Chen, Y. Li, K. Yang, F.H. Wang, The effect of Cu addition on the electrochemical corrosion and passivation behavior of stainless steels, Electrochim. Acta 55 (2010) 5028-5035.
- [25] Z.H. Dan, F.X. Qin, Y. Sugawara, I. Muto, N. Hara, Effects of the initial microstructure of Ti-Cu alloys on final nanoporous copper via dealloying, J. Alloy. Comp. 557 (2013) 166–171.